Neuromelanin-sensitive MRI as a noninvasive proxy measure of dopamine function in the human brain

Clifford M. Cassidy[a,b,1], Fabio A. Zucca[c], Ragy R. Girgis[a], Seth C. Baker[a], Jodi J. Weinstein[a,d], Madeleine E. Sharpe[e,f], Chiara Bellei[c], Alice Valmadre[c], Nora Vanegas[e], Lawrence S. Kegeles[a], Gary Brucato[a], Un Jung Kang[e], David Sulzer[a,e], Luigi Zecca[a,c], Anissa Abi-Dargham[a,d], and Guillermo Horga[a,1]

[a]Department of Psychiatry, New York State Psychiatric Institute, Columbia University Medical Center, New York, NY 10032; [b]University of Ottawa Institute of Mental Health Research, affiliated with The Royal, Ottawa, ON K1Z 8N3, Canada; [c]Institute of Biomedical Technologies, National Research Council of Italy, Segrate, 20090 Milan, Italy; [d]Department of Psychiatry, Stony Brook University, Stony Brook, NY 11794; [e]Department of Neurology, Columbia University Medical Center, New York, NY 10032; and [f]Department of Neurology and Neurosurgery, McGill University, Montreal, QC H3A 2B4, Canada

Neuromelanin-sensitive MRI (NM-MRI) purports to detect the content of neuromelanin (NM), a product of dopamine metabolism that accumulates with age in dopamine neurons of the substantia nigra (SN). Interindividual variability in dopamine function may result in varying levels of NM accumulation in the SN; however, the ability of NM-MRI to measure dopamine function in non-neurodegenerative conditions has not been established. Here, we validated that NM-MRI signal intensity in postmortem midbrain specimens correlated with regional NM concentration even in the absence of neurodegeneration, a prerequisite for its use as a proxy for dopamine function. We then validated a voxelwise NM-MRI approach with sufficient anatomical sensitivity to resolve SN subregions. Using this approach and a multimodal dataset of molecular PET and fMRI data, we further showed the NM-MRI signal was related to both dopamine release in the dorsal striatum and resting blood flow within the SN. These results suggest that NM-MRI signal in the SN is a proxy for function of dopamine neurons in the nigrostriatal pathway. As a proof of concept for its clinical utility, we show that the NM-MRI signal correlated to severity of psychosis in schizophrenia and individuals at risk for schizophrenia, consistent with the well-established dysfunction of the nigrostriatal pathway in psychosis. Our results indicate that noninvasive NM-MRI is a promising tool that could have diverse research and clinical applications to investigate in vivo the role of dopamine in neuropsychiatric illness.

magnetic resonance imaging | dopamine | neuromelanin | schizophrenia | Parkinson's disease

In vivo measurements of dopamine activity are critical for understanding how this key neuromodulator contributes to cognition, neurodevelopment, aging, and neuropsychiatric disease in humans. In medicine, such measurements may result in objective biomarkers that predict clinical outcomes in dopamine-related illness, including Parkinson's disease (PD) and psychotic disorders, ideally by using techniques that capture the underlying pathophysiology while being easy to acquire in clinical settings (1). Here, we conducted a series of validation and proof-of-concept studies to test whether noninvasive, neuromelanin-sensitive MRI (NM-MRI) of the midbrain can provide a proxy marker for activity of midbrain dopamine neurons and capture important pathophysiological phenotypes associated with dysfunction of these neurons.

Neuromelanin (NM) is a dark pigment synthesized via iron-dependent oxidation of cytosolic dopamine and subsequent reaction with proteins and lipids in midbrain dopamine neurons (2). NM pigment accumulates inside specific autophagic organelles, which contain NM-iron complexes, along with lipids and various proteins (3, 4). NM-containing organelles accumulate gradually over the lifespan in the soma of dopamine neurons in the substantia nigra (SN) (2, 4), a nucleus that owes its name to its dark appearance due to the high concentration of NM, and

are only cleared from tissue following cell death through the action of microglia, as in neurodegenerative conditions such as PD (5, 6). Given that NM–iron complexes are paramagnetic (6, 7), they can be imaged using MRI (8–11). A family of MRI sequences, known as NM-MRI, captures groups of neurons with high NM content, such as those in the SN, as hyperintense regions (8, 9). NM-MRI signal is reliably decreased in the SN of patients with PD (8, 10, 12–15), consistent with the degeneration of NM-positive SN dopamine cells (16) and with the decrease in NM concentration in postmortem SN tissue of PD patients compared with age-matched controls (17). While this evidence supports the use of NM-MRI for in vivo detection of SN neuron loss in neurodegenerative illness, direct demonstrations that this MRI technique is sensitive to regional variability in NM concentration even in the absence of neurodegenerative SN pathology are lacking. Furthermore, although induction of dopamine synthesis via L-dopa administration is known to induce NM accumulation in rodent SN cells (18, 19), and although prior work assumed that NM-MRI signal in the SN indexes dopamine neuron function in humans (20, 21), direct evidence is lacking to support the assumption that interindividual differences in dopamine function could lead to MRI-detectable differences in NM accumulation. Critically, such evidence is necessary to support

the utility of NM-MRI for psychiatric and neuroscientific applications beyond those related to neurodegenerative illness.

To support extending the use of NM-MRI for such applications, we present a series of validation studies. A first necessary step was to show that NM-MRI is sensitive enough to detect regional variability in tissue concentration of NM, which presumably depends on interindividual and interregional differences in dopamine function (including synthesis and storage capacity), and not just to loss of NM-containing neurons due to neurodegeneration. To test this, we compared MRI measurements to neurochemical measurements of NM concentration in postmortem tissue without neurodegenerative SN pathology. Because variability in dopamine function may not occur uniformly throughout all SN tiers (22–26), the next necessary step was to show that NM-MRI, which has high anatomical resolution compared with standard molecular-imaging techniques, has sufficient anatomical specificity. To this end, we used NM-MRI in its established role as a marker of degeneration in PD to test the ability of a voxelwise approach to capture the known topographical pattern of cell loss within the SN in the illness (27, 28). The critical next step was then to provide direct evidence for a relationship between NM-MRI and dopamine function using the voxelwise approach. To test this, we correlated NM-MRI signal to a well-validated PET measure of dopamine release into the striatum—the main projection site of SN neurons—and to a fMRI measure of regional blood flow in the SN, an indirect measure of activity in SN neurons, in a group of individuals without neurodegenerative illness. Finally, we tested a potential application of NM-MRI for nonneurodegenerative psychiatric illness [i.e., illness without known neurodegeneration at the cellular level (24, 29)]: we used this technique in unmedicated patients with schizophrenia and individuals at clinical high risk (CHR) for psychosis to test the ability of NM-MRI to capture a psychosis-related functional phenotype consisting of nigrostriatal dopamine excess.

Results

Validation of NM-MRI as a Proxy Measure of Dopamine Function.

Relationship to NM concentration in postmortem midbrain tissue. We first set out to test whether NM-MRI is sensitive to variation in NM tissue concentration at levels found in individuals without major neurodegeneration of the SN, a prerequisite for its use as a marker of interindividual variability in dopamine function in healthy and psychiatric populations. To this end, we validated it against gold-standard measures of NM concentration by scanning SN-containing midbrain sections from seven individuals without histopathology compatible with PD or PD-related syndromes (including absence of Lewy bodies composed of abnormal protein aggregates) using a NM-MRI sequence. After scanning, each specimen was dissected along gridline markings into 13–20 grid sections (*Methods*). In each grid section, we measured tissue concentration of NM using biochemical separation and spectrophotometry determination and also calculated the averaged NM-MRI contrast-to-noise ratio (CNR) across voxels within the grid section (Fig. 1 *A–D*). Across all midbrain specimens, grid sections with higher NM-MRI CNR had higher tissue concentration of NM ($\beta_1 = 0.56$, $t_{114} = 3.36$, $P = 0.001$, mixed-effects model; 116 grid sections, seven specimens: Fig. 1 *E* and *F*; see *SI Appendix* for statistical methods). As expected, hyperintensities were most apparent in grid sections corresponding with the NM-rich SN. However, similar to in vivo NM-MRI images (Figs. 2 and 3), posterior-medial regions of the midbrain around the periaqueductal gray (PAG) area tended to appear hyperintense despite relatively low concentrations of NM. Although we could not account for the source of this hyperintensity, controlling for the presence of PAG in grid sections (PAG content) improved the correspondence of NM-MRI CNR to NM concentration in non-PAG regions ($\beta_1 = 1.03$, $t_{112} =$
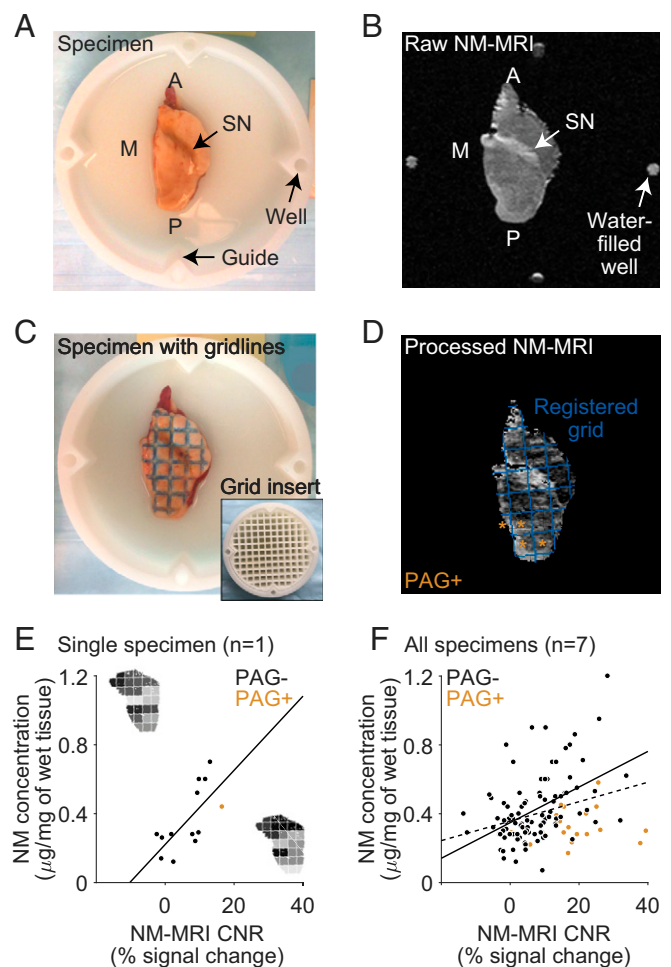

Fig. 1. NM-MRI CNR correlates with NM concentration across sections of postmortem midbrain tissue from individuals without PD pathology. An axial view of a postmortem specimen of the right hemimidbrain is shown in photographic images (*A* and *C*) and NM-MRI images (*B* and *D*). The specimen is immersed in MRI-invisible lubricant (Fomblin perfluoropolyether Y25), contained within a custom dish. Arrows in *A* and *B* highlight the location of the SN, which appears as a dark band in *A* and as a hyperintense band in *B*. Dye gridlines were applied to the specimen (*C*) using the grid insert (shown in the dish in *C*, *Inset*) as a stamp. These gridlines were used to dissect the specimen into grid sections. NM-MRI CNR measurements were averaged in the same grid sections after image processing (*D*). Well markers shown at the four cardinal points in *B* were used in the registration of the grid, shown in blue in *D* superimposed on the preprocessed NM-MRI image averaged across sections. Grid sections containing the periaqueductal gray (PAG) are indicated by tan asterisks. (*E*) Scatterplot displaying the correlation between NM concentration and NM-MRI CNR for a single specimen. Grid-map *Insets* of this specimen displayed beside the axes indicate NM concentration (*Top Left* by *y* axis) and NM-MRI CNR (*Bottom Right* by x-axis) according to a normalized grayscale for each grid section. (*F*) Scatterplot displaying the correlation between NM concentration and NM-MRI CNR for all seven specimens. Tan data points represent sections including the PAG, where CNR was less strongly correlated with NM concentration. The discontinuous line represents the linear fit of all data points across all grid sections and specimens, including PAG+ sections. The continuous line represents the linear fit excluding the PAG+ sections. A, anterior; M, medial; P, posterior.

5.51, $P = 10^{-7}$). Under this model, a 10% increase in NM-MRI CNR corresponds with an estimated increase of 0.10 μg of NM per mg of tissue.

The relationship between NM-MRI CNR and NM concentration remained ($\beta_1 = 0.45$, $t_{111} = 2.15$, $P = 0.034$) in an extended model controlling for the proportion of SN voxels within each
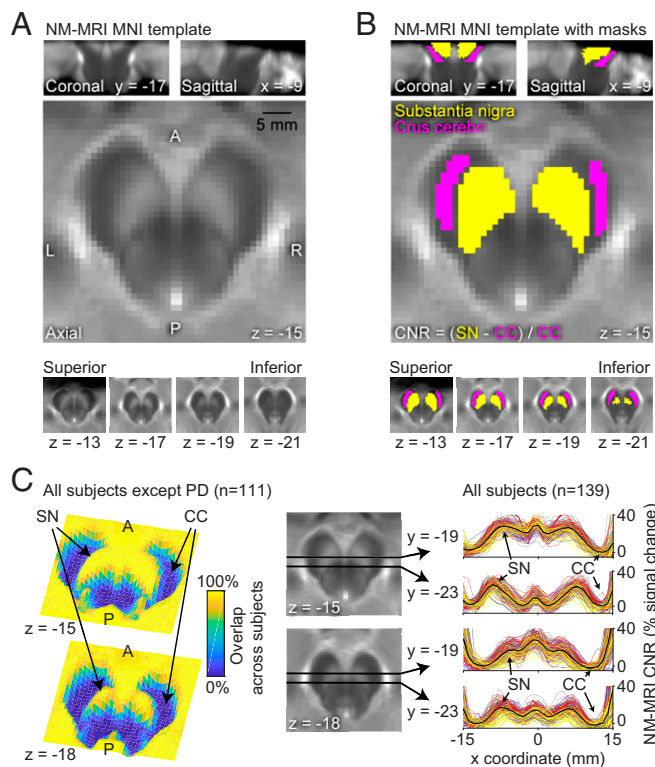
Fig. 2. Spatial normalization and anatomical masks for voxelwise analysis on NM-MRI images. (*A*) Template NM-MRI image created by averaging the spatially normalized NM-MRI images from 40 individuals in MNI space. Note the high signal intensity in the SN and moderate intensity in the PAG area. (*B*) Masks for the SN (yellow voxels) and the crus cerebri (CC) (pink voxels) reference region (used in the calculation of CNR) are overlaid onto the template in *A*. These anatomical masks were made by manual tracing on the NM-MRI template. (*C*) Quality checks for spatial normalization of NM-MRI images. Overlap 3D images on the *Left* indicate the percentage of subjects with spatially overlapping signal in SN and outside the midbrain for a superior ($z = -15$) and an inferior ($z = -18$) slice. These images were made by creating binary maps of each subject's preprocessed NM-MRI image (thresholded at CNR = 10%) and calculating the percentage of overlap for each voxel across all subjects without neurodegenerative disease (PD subjects were excluded given the manifest signal decreases, which can be seen in overlap images for this group in *SI Appendix*, Fig. S1). Lines plotted on the *Right* show a consistent CNR landscape over the *x* coordinate [from left ($x = -15$) to the midline ($x = 0$) and to the right ($x = +15$)] for normalized NM-MRI images in all study subjects; two plots [one for an anterior ($y = -19$) and one for a posterior ($y = -23$) line] are shown for each of two slices, as indicated by axial midbrain images in the *Center*. The location of the left SN (first peak from the left) and right CC (last trough from the left) is indicated by arrows and plotted lines are color-coded by group (gray: healthy controls; yellow: PD patients; red: schizophrenia patients; blue: CHR individuals; black: average of all subjects), which highlight the consistency of these landmarks in normalized images across subjects. A, anterior; L, left; P, posterior; R, right.

grid section (and again for PAG content). This latter result suggests that NM-MRI CNR explains variance in NM concentration in the SN and surrounding areas beyond that explained simply by the increase in both measures in SN compared with non-SN voxels, an increase that would be expected even if NM-MRI could only localize the SN without measuring regional NM concentration. These results thus indicate that NM-MRI signal corresponds to regional tissue concentration of NM, particularly in the midbrain region surrounding the SN, the region our subsequent in vivo studies focused on. All results held after excluding one specimen in which the neuropathological examination found decreased neuronal density in the SN despite lack of evidence for PD-related pathology (extended model:

$\beta_1 = 0.46$, $t_{96} = 2.20$, $P = 0.030$), further confirming that the relationship between NM-MRI and NM concentration was not driven by reduced cell counts.

Validation of voxelwise approach. Having shown that NM-MRI measures regional concentration of NM in and around the SN, we then aimed to establish whether regional differences in NM-MRI signal capture biologically meaningful variation across anatomical subregions within the SN. This was necessary for our ultimate objective of using this tool to interrogate dopamine function, since the heterogeneity of cell populations in the SN (22–26) suggests that dopamine function may differ substantially between neuronal tiers projecting to ventral striatum, dorsal striatum, or cortical sites. We reasoned that a voxelwise analysis within the SN may be sensitive to processes affecting specific subregions or likely discontinuous neuronal tiers within the SN (23) (see Fig. 2 and *SI Appendix*, Fig. S1 for information regarding spatial normalization and anatomical masks used in voxelwise analyses). Supporting the feasibility of this approach, the majority of individual SN voxels exhibited good-to-excellent test–retest reliability (*SI Appendix*, Fig. S2), extending similar demonstrations at the region level (30). To test the anatomical specificity of the voxelwise NM-MRI approach, we capitalized on the well-established ability of NM-MRI to detect neurodegeneration in PD and the known topography of cell loss in the illness. Previous PD work has shown decreases in NM concentration (16, 17) and in NM-MRI signal in the whole SN (8, 15) and lateral regions of bisected SN (12–14). Histopathological studies of the SN further support a topographical progression of PD pathology that preferentially affects lateral, posterior, and ventral subregions of SN in mild-to-moderate disease stages (27, 28). Using NM-MRI data in 28 patients diagnosed with mild-to-moderate PD and 12 age-matched controls (see *SI Appendix*, Table S2 for sample characteristics), we thus tested whether a voxelwise analysis would capture this topographic pattern. PD patients had significantly lower NM-MRI CNR compared with control individuals (439 of 1,807 SN voxels at $P < 0.05$, robust linear regression adjusting for age and head coil; $P_{corrected} = 0.020$, permutation test; peak voxel Montreal Neurological Institute (MNI) coordinates [*x*, *y*, *z*]: −6, −18, −18 mm; *SI Appendix*, Fig. S3). Critically, our approach was able to capture the known anatomical topography of dopamine neuron loss within the SN (27, 28) (Fig. 3*B*): larger CNR decreases in PD tended to predominate in more lateral ($\beta_{|x|} = -0.13$, $t_{1,803} = -14.2$, $P = 10^{-43}$), posterior ($\beta_y = -0.05$, $t_{1,803} = -6.6$, $P = 10^{-10}$), and ventral SN voxels [$\beta_z = 0.17$, $t_{1,803} = 16.3$, $P = 10^{-55}$, multiple linear regression analysis predicting *t* statistic of group difference across SN voxels as a function of their coordinates in *x* (absolute distance from the midline), *y*, and *z* directions: omnibus $F_{3;1,803} = 111$, $P = 10^{-65}$].

Relationship of NM-MRI signal to dopamine function. Having validated the anatomical sensitivity of our voxelwise approach, we then proceeded to test whether NM-MRI signal in the SN correlated with dopamine function in vivo. To that end, we used PET imaging to measure dopamine-release capacity (ΔBP_{ND}) as the change in binding potential of the dopamine D2/D3 receptor radiotracer [^{11}C]raclopride between baseline and following administration of dextroamphetamine (0.5 mg/kg, PO). This method measures the release of dopamine from the presynaptic sites of dopamine axons, including its vesicular and cytosolic pools (31, 32), into striatal synapses, so it is relevant to our hypothesis that (trait-like) interindividual differences in the magnitude of these dopamine pools are a key determinant of NM accumulation (19, 31). We collected data in a group of 18 individuals without neurodegenerative illness, which included 9 healthy controls and 9 unmedicated patients with schizophrenia. As a first approximation, to show a global relationship between NM-MRI signal and dopamine-release capacity, we performed a region-of-interest (ROI)-based correlation of mean
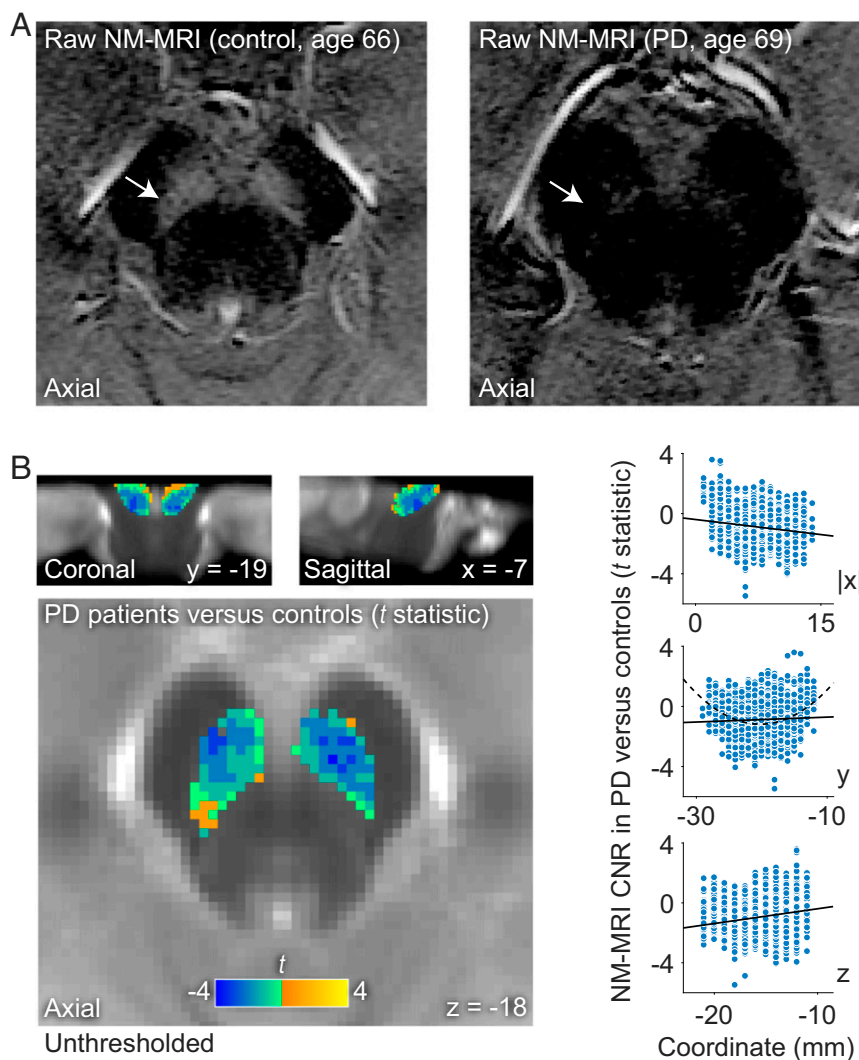
Fig. 3. Voxelwise NM-MRI analysis are sensitive to topographic patterns of NM variation within the SN. (*A*) Raw NM-MRI images of the midbrain (intensity-normalized to the respective CC reference regions and with identical contrast adjustments for visualization purposes). The SN, indicated by arrows, has markedly higher signal in a healthy control (*Left*) compared with a patient with PD (*Right*). (*B*) *t*-statistic map of the SN showing the size of the signal decrease in NM-MRI CNR in PD compared with matched controls (with darker blue values indicating more negative *t*-statistic values and greater decreases in PD and lighter yellow values indicating more positive *t*-statistic values and greater increases in PD, relative to controls) overlaid onto the NM-MRI template. This decrease was more pronounced in more lateral, posterior, and ventral SN voxels, as denoted in the map by the location of darker blue voxels and as shown in the scatterplots on the *Right* (each data point is one voxel in the SN mask). Continuous lines in the scatterplots indicate the linear fit of the relationship between the anatomical location of each voxel, in the *x* (absolute *x* coordinates with respect to the midline) (*Top Right*), *y* (*Middle Right*), and *z* (*Bottom Right*) directions and the *t*-statistic of the group difference between PD and controls. For the *y* direction, a discontinuous curve shows the quadratic fit, which describes well the relationship between *y* coordinate and *t*-statistic values. These topographic relationships were not driven by voxels at the edges of the SN mask since eroding the boundaries of the mask did not impact the results.

NM-MRI CNR in the whole SN and mean ΔBP_{ND} in the whole striatum and found that individuals with higher NM-MRI signal had greater dopamine-release capacity (Spearman $\rho = 0.64$, 95% CI = 0.26–0.87, $P = 0.013$, partial correlation adjusting for diagnosis, age, head coil, and incomplete SN coverage; *Methods*). To examine subregional effects, we focused on dopamine release in the associative striatum, part of the dorsal striatum. We selected this subregion to ensure sufficient variability, as patients with schizophrenia tend to exhibit the greatest excess in dopamine release here (33). Also, the dorsal striatum receives projections from the SN (via the nigrostriatal pathway), while the ventral striatum receives projections predominantly from the ventral tegmental area (via the mesolimbic pathway) (22, 23), which is more difficult to visualize in NM-MRI scans due to its lower NM concentration (16) and smaller size. A voxelwise analysis was performed in which, for each subject, ΔBP_{ND} was measured and correlated to NM-MRI CNR in the SN mask at each voxel. This revealed a set of SN voxels where NM-MRI CNR correlated positively with dopamine-release capacity in the associative striatum [225 of 1,341 (see below) SN voxels at $P < 0.05$, Spearman partial correlation adjusting for diagnosis, age, and head coil; $P_{corrected} = 0.042$, permutation test; peak voxel MNI coordinates [x, y, z]: −1, −18, −16 mm; Fig. 4*A*]. This effect exhibited a topographic distribution such that voxels related to dopamine release tended to predominate in anterior and lateral aspects of the SN (*SI Appendix*). This analysis was performed

in a smaller SN mask (1,341 voxels) because relatively few subjects had usable data in the dorsal-most SN (*SI Appendix*). No interaction with diagnosis was found ($P = 0.31$). Significant effects were also obtained in exploratory voxelwise analyses of dopamine-release capacity in other striatal subdivisions (except the motor striatum; see *SI Appendix*, Table S4).

Relationship of NM-MRI signal to neural activity in the SN. Since the latter results indicated that individuals with higher dopamine release from nigrostriatal SN neurons had higher NM accumulation, as measured via NM-MRI, we reasoned that NM accumulation would also correlate with local trait-like tendency for increased activity in SN neurons. To test this, we used arterial spin-labeling fMRI (ASL-fMRI) to measure regional cerebral blood flow (CBF), a well-established (indirect) functional measure of neuronal activity (34–37) that captures trait-like interindividual differences in resting activity (38). We indeed found that among 31 individuals without neurodegenerative illness (12 healthy individuals, 19 schizophrenia patients), higher CBF in the SN correlated with higher SN NM-MRI CNR. This was true in ROI analyses averaging values in SN voxels related to dopamine-release capacity ("dopamine voxels," $r = 0.40$, 95% CI = 0.08–0.66, $P = 0.030$, partial correlation controlling for age and diagnosis; Fig. 4*B*) and in the whole SN ($r = 0.48$, 95% CI = 0.19–0.75, $P = 0.008$, partial correlation controlling for age, diagnosis, and incomplete SN coverage). Again, no interactions with diagnosis were found (all $P > 0.7$). We failed to find correlations between SN NM-MRI CNR and CBF averaged in the
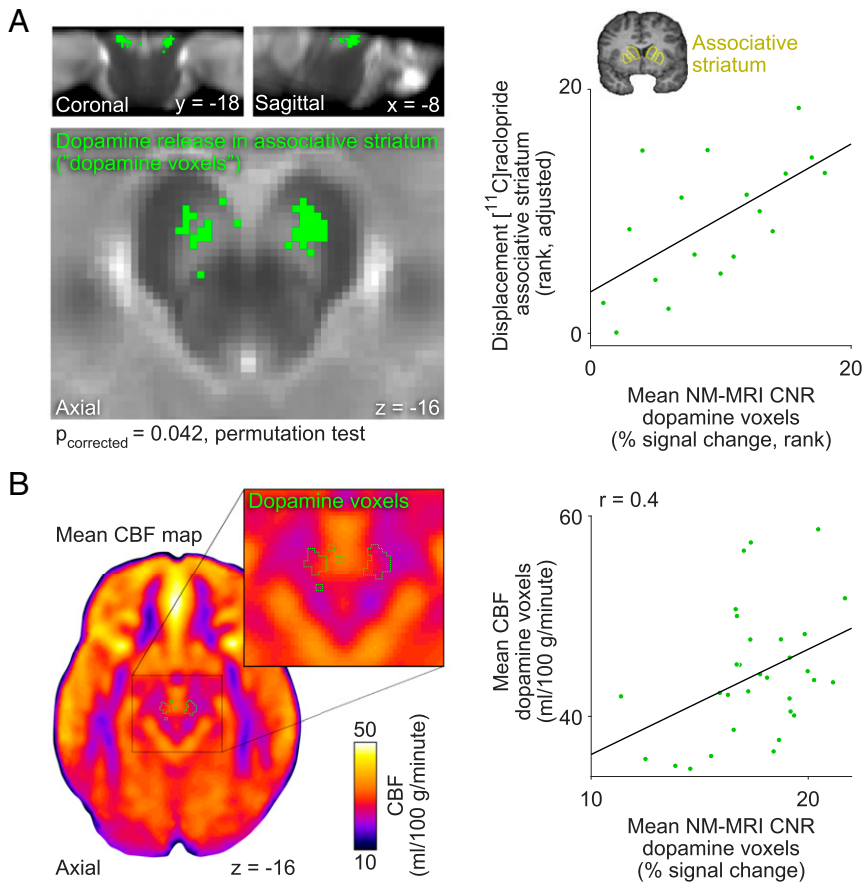
Fig. 4. NM-MRI CNR correlates with measures of dopamine function across individuals without neurodegenerative illness. (*A*) Map of SN voxels where NM-MRI CNR positively correlated (thresholded at $P < 0.05$, voxel level) with a PET measure of dopamine-release capacity in the associative striatum (green voxels) overlaid on the NM-MRI template image. The scatterplot on the *Right* shows NM-MRI CNR extracted from the significant voxels in *A* (with values ranked, consistent with a nonparametric analysis), plotted against dopamine-release capacity in the associative striatum ([^{11}C]raclopride displacement after amphetamine administration; ranked values). These plotted data showed a (biased) effect size of $\rho = 0.69$; the unbiased effect size, calculated via a leave-one-out procedure (*SI Appendix*), was $\rho = 0.62$ (95% CI = 0.14–0.86). Coronal view of anatomical image by the *y* axis of the scatterplot shows the location of the associative striatum (yellow outline), manually traced on a representative subject's T1 anatomical image. (*B*) Mean resting CBF map derived from 31 individuals (axial view). *B, Inset* shows detail of the midbrain with a green outline indicating the location of the SN voxels where NM-MRI CNR was related to dopamine-release capacity (the voxels shown in solid green in *A*). The scatterplot on the *Right* shows the correlation of resting CBF extracted from these voxels to NM-MRI CNR extracted from these same voxels (note that voxel selection is unbiased here).

crus cerebri reference region ($P = 0.10$) or the whole-brain gray matter ($P = 0.30$), consistent with our hypothesis that NM accumulation is related to local activity in the SN (rather than to activity in other brain regions).

Relationship of NM-MRI to Psychosis. Psychosis is associated with excessive dopamine-release capacity and dopamine-synthesis capacity in the striatum (23, 33) in the absence of neurodegeneration of SN neurons (24, 29). This dopamine dysfunction is particularly prominent in the associative striatum—which receives projections from discontiguous regions of dorsal and ventral SN tiers through the nigrostriatal pathway (23)—and is present in schizophrenia (33), at-risk populations for psychosis (39, 40), and bipolar disorder (41), suggesting a dimensional relationship to psychotic symptoms rather than a specific relationship to schizophrenia or other diagnostic categories. Given this and the evidence presented above supporting that NM-MRI signal indexes dopamine function, we hypothesized that excess dopamine in SN neurons would result in more accumulation of NM [in the body of those neurons in the SN (3)] in individuals with more severe syndromal or subsyndromal psychotic symptoms (among patients with schizophrenia and among individuals at CHR for psychosis, respectively; see *SI Appendix* for sample characteristics and description of clinical measures). Indeed, we found that more severe (syndromal) psychotic symptoms in patients with schizophrenia (PANSS-PT scores, $n = 33$) and more severe attenuated (subsyndromal) psychotic symptoms in CHR individuals (SIPS-PT scores, $n = 25$) both correlated with higher NM-MRI CNR in overlapping SN voxels (45 voxels; $P_{corrected} = 0.00001$, permutation test for conjunction effect; Fig. 5). This effect exhibited a topographic distribution such that psychosis-overlap voxels tended to predominate in ventral and anterior aspects of

the SN (*SI Appendix*). Correlations between NM-MRI CNR in these psychosis-overlap voxels and severity of psychosis were specific to positive symptoms of psychosis in schizophrenia ($r = 0.38$, 95% CI = 0.12–0.62, $P = 0.044$) and CHR [$r = 0.57$, 95% CI = 0.35–0.78, $P = 0.006$, partial correlations controlling for negative-symptom scores (PANSS-NT or SIPS-NT, respectively), general-symptom scores (PANSS-GT or SIPS-GT, respectively), age, and head coil]. Based on our calibrations with measurements of NM concentration in postmortem tissue, the estimated difference of NM concentrations in the psychosis-overlap voxels between individuals with the least severe versus the most severe psychotic symptoms would be 0.38 μg/mg versus 0.67 μg/mg in schizophrenia (estimated concentrations for PANSS-PT scores of 10 versus 29) and 0.31 μg/mg versus 0.62 μg/mg in CHR (estimated concentrations for SIPS-PT scores of 9 versus 21). Although our main aim here was to identify correlates of psychosis rather than of diagnostic categories, we also compared the groups and found no significant differences between the schizophrenia and CHR groups or between either of these groups and matched healthy control groups (although highly psychotic patients did show higher NM-MRI signal than controls; see *SI Appendix*). This is consistent with the notion that the nigrostriatal-dopamine phenotype—at least as captured by NM-MRI—represents a dimensional correlate of psychosis rather than a categorical correlate of diagnosis.

Although we failed to find a significant overlap between psychosis-overlap voxels and those exhibiting a correlation with dopamine-release capacity in the associative striatum (6 voxels; $P_{corrected} = 0.62$, permutation test for conjunction), we found a significant overlap between voxels where NM-MRI CNR correlated with psychosis in schizophrenia and voxels where NM-MRI CNR correlated with dopamine-release capacity in this striatal

subregion (80 voxels; $P_{corrected}$ = 0.002, permutation test for conjunction). This suggests that (syndromal) psychosis relates to increased NM accumulation in portions of the SN where NM accumulation specifically reflects increased dopamine in the nigrostriatal pathway.

Discussion

We have presented data validating the use of NM-MRI as a measure of NM concentration in the SN, beyond its use as a marker of neuronal loss in neurodegenerative illness. Consistent with previous preclinical work showing that increased dopamine availability in SN dopamine neurons results in NM accumulation in the soma (18, 19), we found that an in vivo molecular-imaging readout of dopamine function in these neurons (i.e., striatal dopamine-release capacity) correlates with NM-MRI signal in a subregion of the SN among humans without neurodegenerative illness. CBF in the same subregion of the SN also correlated with local increases of NM-MRI CNR, similarly consistent with a link between neural activity in SN and NM accumulation. Altogether, converging evidence from various experiments and different datasets strongly suggests that NM-MRI signal in the SN provides a proxy measure for function of dopamine neurons in this midbrain region, particularly in neuronal tiers of the SN that project to the dorsal striatum via the nigrostriatal pathway (22, 23).

We believe this work represents a significant methodological advance in that we provided a validation of NM-MRI measures against a number of gold-standard and well-validated methods [including high-quality biochemical (17), PET imaging (42, 43), and clinical measurements (44, 45)] and developed an automated method for regional interrogation of NM-MRI signal within the SN. First, our postmortem experiment employed an approach for accurate determination of NM concentration across multiple tissue sections throughout the midbrain, which allowed us to confirm the ability of NM-MRI to measure regional concentration of NM and to calibrate the NM-MRI signal in subsequent in vivo studies, in line with previous recommendations (17). Prior work has shown that the NM-MRI contrast mechanism in synthetic NM phantoms depends on the influence of iron-bound melanic NM components on T1-relaxation time and magnetization-transfer ratio (9, 11) and that NM-MRI signal in postmortem tissue correlates with the density of NM-containing neurons in the SN (46, 47). Our approach allowed us to build on this work by showing that the NM-MRI signal reflects the concentration of NM in tissue,

rather than solely reflecting the presence or number of NM-containing SN neurons. Because this observation was apparent in the absence of neurodegeneration of SN neurons, it opened the possibility that NM-MRI measures of NM concentration could be used as a proxy for dopamine function. Second, we developed a voxelwise method that we validated in a cohort of patients with PD, which, consistent with prior work (8, 10, 12–15), exhibited a robust reduction of SN CNR, by showing that our method further revealed a regional pattern of SN signal reduction, consistent with the known topographical pattern of neuronal loss in the disease (27, 28). Future studies should directly test this voxelwise method against conventional analysis methods of NM-MRI to determine its ability to enhance classification of PD patients, especially at early or premanifest stages of the illness. This voxelwise method not only may increase the precision and sensitivity of NM-MRI measures but, by virtue of using a standardized space, may also minimize circularity in ROI definitions (10) and spatial variability between subjects and studies. Third, we established a correlation between NM-MRI measures against a well-validated measure of dopamine function in vivo: a PET measure of amphetamine-induced dopamine release that is thought to reflect the available pools of vesicular and cytosolic dopamine in presynaptic dopamine neurons projecting to the striatum. This measure was well-suited to build on preclinical evidence that increased availability of cytosolic dopamine drives NM accumulation (18, 19), but future work should replicate the observed relationship between NM-MRI and this measure and examine relationships with measures of dopamine-synthesis capacity. Prior work using different PET dopamine measures in a small sample of young healthy individuals found a correlation between NM-MRI measures and dopamine D2-receptor density in the SN, but not to dopamine-synthesis capacity in the midbrain (via a dopa measure) (48). However, such a small and homogeneous sample of young individuals is unlikely to show substantial variability in dopamine function or NM accumulation and may have thus hampered the sensitivity of this study to detect an effect, an issue that we circumvented here by including individuals with a larger age range and some with dopamine dysfunction (i.e., patients). Limitations of PET measures of dopa in the midbrain (49) could have also played a role.

By showing that NM-MRI could capture the established dopamine dysfunction associated with psychosis, we provided convergent evidence for the relationship between NM-MRI and
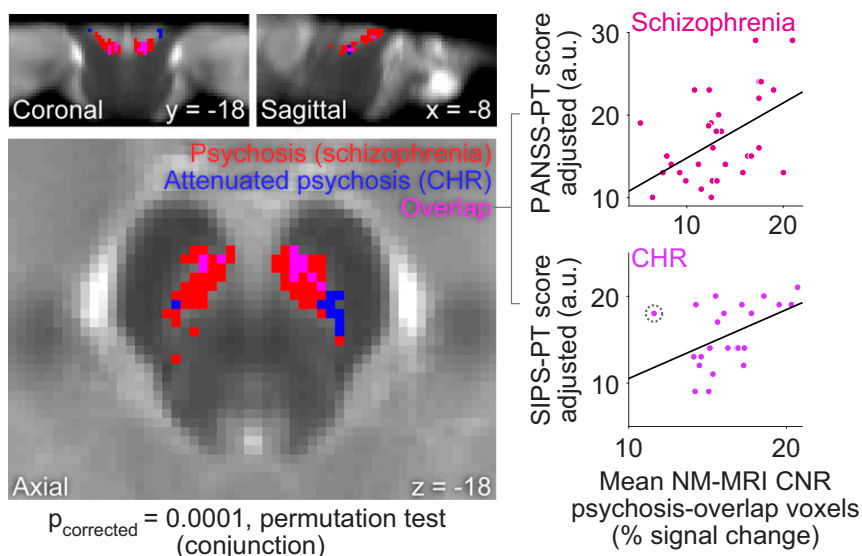

Fig. 5. NM-MRI CNR correlates with the severity of psychotic symptoms. The map on the *Left* shows SN voxels where NM-MRI CNR was positively correlated with the severity of psychotic symptoms (thresholded at $P < 0.05$, voxel level) in patients with schizophrenia (red voxels) or with the severity of attenuated psychotic symptoms in individuals at CHR for psychosis (blue voxels). The "psychosis-overlap" voxels where both effects are present are displayed in pink. Scatterplots on the *Right* show the correlation of mean NM-MRI CNR extracted from psychosis-overlap voxels with severity of psychotic symptoms in patients with schizophrenia ($r = 0.52$) (*Top Right*) and attenuated psychotic symptoms in CHR individuals ($r = 0.48$) (*Bottom Right*). (Note that our approach here of extracting signal from a conjunction mask derived from two separate cohorts of individuals should reduce but may not eliminate the bias in these effect-size estimates.) Analysis of this relationship in CHR revealed an influential outlier data point [shown encircled by a dotted line; Cook's distance = 0.61, cutoff (4/n) = 0.16] that counteracted the overall group trend. When eliminating this data point, the strength of the correlation increased from $r = 0.48$ to $r = 0.64$.

dopamine function in the nigrostriatal pathway as well as support for its potential value as a research tool and candidate biomarker for psychosis. Because postmortem studies have found normal counts of SN dopamine neurons in psychotic patients (24, 29) together with abnormal markers of dopamine function in these neurons (24, 50, 51) (but see ref. 52), increased NM-MRI signal in more severely psychotic individuals likely reflects psychosis-related alterations in dopamine function. This interpretation is also consistent with PET research in psychosis, which has reliably identified robust increases in dopamine tone in presynaptic dopamine neurons projecting to the striatum, and in particular in nigrostriatal neurons projecting to the dorsal associative striatum (23, 33). This phenotype has been identified in patients with psychotic disorders—including schizophrenia and bipolar disorder—in proportion to the severity of their psychotic symptoms (41, 53). This dopamine phenotype has also been reported in individuals at high risk for psychosis, particularly in those who go on to develop a psychotic disorder (39, 40). Our work suggests that this psychosis-related phenotype consisting of nigrostriatal dopamine excess results in an increase in NM accumulation in the SN that can be captured with NM-MRI. Specifically, we found a (mostly) ventral SN subregion where NM-MRI CNR is increased in proportion to severity of psychosis in schizophrenia and to severity of attenuated psychosis in CHR individuals. This mostly ventral subregion of SN (at least as defined in patients with schizophrenia alone) exhibited a relationship to dopamine function in the dorsal associative striatum, consistent with the dense projections of the ventral SN tier to this striatal region (23). Perhaps surprisingly, exploratory analyses failed to detect group differences in NM-MRI CNR between CHR individuals, patients with schizophrenia, and healthy individuals (*SI Appendix*). Consistent with other evidence that dopamine dysfunction is more closely related to psychosis than to schizophrenia (41, 53), our data thus support that NM-MRI captures a psychosis-related (but not necessarily diagnosis-specific) dysfunction in the nigrostriatal dopamine pathway, with this phenotype emerging before the development of full-blown schizophrenia. In contrast, some previous studies found a significant increase in NM-MRI CNR in individuals with schizophrenia (20, 21) (but see refs. 54 and 55) but failed to observe a significant relationship between NM-MRI signal and severity of psychotic symptoms (20, 55). This inconsistency may be explained by the inclusion of patients treated with antidopaminergic medication in these studies. Inclusion of medicated patients is likely to mask dopaminergic correlates of psychotic symptoms, perhaps by exposing treatment-refractory patients in whom nondopaminergic alterations may predominate (56) or perhaps via direct effects of antipsychotic medication on NM accumulation, as some antipsychotics may accumulate in NM organelles (57) and exhibit a dose-dependent relationship with NM-MRI signals (21).

Altogether, our findings further underscore the promise of NM-MRI as a clinically useful biomarker for nonneurodegenerative conditions associated with dopamine dysfunction. It has the obvious advantages of being practical (inexpensive and noninvasive), particularly for pediatric and longitudinal imaging, and of providing high anatomical resolution compared with standard molecular imaging methods, which allows it to resolve functionally distinct SN tiers with different pathophysiological roles (22–26). The presumed ability of NM-MRI to index long-term dopamine function, given the slow accumulation of NM in the SN over the lifespan (7, 17), and the high reproducibility of this technique (30) suggest that NM-MRI may be a stable marker insensitive to acute states (e.g., recent sleep loss or substance consumption). This is a particularly appealing characteristic for a candidate biomarker and one that could complement other markers such as PET-derived measures, which, in contrast, may better reflect state-dependent dopamine levels (53). In this light, the lack of significant differences between schizophrenia or CHR and health, together with the observed correlation

with severity of psychosis, could suggest that NM-MRI better captures a longer-term propensity for psychosis (compared with more acute psychosis-related states captured by PET measures of dopamine function). Regardless of this, a dimensional marker of psychosis-related dopamine dysfunction may be extremely helpful as a risk biomarker of psychosis. Such a biomarker could further help select a subset of at-risk individuals who, more so than CHR individuals as a whole (58, 59), may benefit from antidopaminergic medication, thus augmenting current risk-prediction algorithms based solely on nonbiological measures (60). Further work is also needed to unveil the full potential of NM-MRI, including applications related to other dopamine-related conditions such as addiction, attention-deficit/hyperactivity disorder, and bipolar disorder, and to other catecholamines, particularly norepinephrine. NM–metal complexes also accumulate from oxidation of norepinephrine in the locus coeruleus (7, 61), a nucleus relevant to stress and anxiety disorders (62, 63) as well as to PD and Alzheimer's disease (64). Our findings supporting NM-MRI signal in the SN as a measure of dopamine function hint at the notion that NM-MRI signal in the locus coeruleus could be a measure of norepinephrine function, but despite some indirect support for this notion (62, 63, 65, 66), further work is needed to directly confirm this.

There are some limits to the potential applications of NM-MRI. As implied above, NM-MRI measures may be ideally avoided in (chronically) medicated patients until antipsychotic effects on NM are better understood. Similar to other neuroimaging measures, our data show that the NM-MRI signal is sensitive but not fully specific to NM concentration. Other tissue properties, including proton density, may impact the signal. Thus, caution in interpreting all changes in NM-MRI signal as changes in NM concentration is warranted, especially in regions with low NM concentration. Future work should further refine methods of acquisition and analysis of NM-MRI data, including methods for correction of motion artifacts known to be problematic for other MRI modalities (67). In correlating resting CBF to NM-MRI signal, we took SN CBF to reflect (trait-like) dopamine–neuron activity, despite the lack of direct evidence supporting this, because CBF measures neural activity (34–37) and the vast majority of human SN neurons are dopaminergic (68). In exploratory analyses, we observed significant correlations of NM-MRI signal to dopamine-release capacity in all striatal subregions except the motor striatum (*SI Appendix*, Table S4). While a failure to detect this correlation in exploratory analyses may not be particularly informative or surprising [given, in part, the constrained range of signal in motor subregions that would be expected in our sample (33) and the differential sources of noise affecting these subregions, including the variable coverage of dorsal SN (*SI Appendix*), which could disproportionately affect motor projections (69)], we cannot conclude that the relationship between NM-MRI signal and dopamine function generalizes to all midbrain dopamine pathways based on the current study alone. Finally, our finding of a relationship between NM-MRI signal and dopamine-release capacity relied on pooling data from individuals with schizophrenia and healthy individuals to widen the signal range. Although we found no evidence for differences in this relationship by group, future studies confined to healthy individuals would be advisable to confirm this relationship in health.

Here, we have presented evidence supporting the use of the NM-MRI signal as a proxy for function of SN dopamine neurons. We have also presented initial evidence supporting the use of NM-MRI to capture the dopamine dysfunction linked to psychosis. Future work should aim to expand these findings to promote development of this candidate biomarker for psychosis risk and treatment selection. Moreover, if our findings are confirmed in diverse populations, this easy-to-acquire and noninvasive MRI technique may have broad applications to investigate neurodevelopment and normative neurocognitive processes throughout the lifespan.

Methods

This study was approved by the Institutional Review Boards of the New York State Psychiatric Institute (NYSPI) and Columbia University. All participants provided written informed consent.

NM-MRI Acquisition. Magnetic resonance (MR) images were acquired for all study participants on a GE Healthcare 3T MR750 scanner using a 32-channel, phased-array Nova head coil. For logistical reasons, a few scans (17% of all scans, 24 out of a total of 139) were acquired using an 8-channel Invivo head coil instead. During piloting, we compared various NM-MRI sequences and achieved optimal CNR (see below for calculation) in the SN using a 2D gradient response echo sequence with magnetization transfer contrast (2D GRE-MT) (70) with the following parameters: repetition time (TR) = 260 ms; echo time (TE) = 2.68 ms; flip angle = 40°; in-plane resolution = 0.39 × 0.39 mm^2; partial brain coverage with field of view (FoV) = 162 × 200; matrix = 416 × 512; number of slices = 10; slice thickness = 3 mm; slice gap = 0 mm; magnetization transfer frequency offset = 1,200 Hz; number of excitations (NEX) = 8; acquisition time = 8.04 min. The slice-prescription protocol consisted of orienting the image stack along the anterior-commissure–posterior-commissure line and placing the top slice 3 mm below the floor of the third ventricle, viewed on a sagittal plane in the middle of the brain. This protocol provided coverage of SN-containing portions of the midbrain (and cortical and subcortical structures surrounding the brainstem) with high in-plane spatial resolution using a short scan easy to tolerate by clinical populations. Whole-brain, high-resolution structural MRI scans were also acquired for preprocessing of the 2D GRE-MT (NM-MRI) data: a T1-weighted 3D BRAVO sequence (inversion time = 450 ms, TR ~ 7.85 ms, TE ~ 3.10 ms, flip angle = 12°, FoV = 240 × 240, matrix = 300 × 300, number of slices = 220, isotropic voxel size = 0.8 mm^3) and a T2-weighted CUBE sequence (TR = 2.50 ms, TE ~ 0.98 ms, echo train length = 120, FoV = 256 × 256, number of slices = 1, isotropic voxel size = 0.8 mm^3). Quality of NM-MRI images was visually inspected for artifacts immediately upon acquisition, and scans were repeated when necessary, time permitting. Ten participants were excluded due to clearly visible, smearing or banding artifacts affecting the midbrain (due to participant motion, $n = 4$), or incorrect image-stack placement ($n = 6$).

NM-MRI Preprocessing. NM-MRI scans were preprocessed using SPM12 to allow for voxelwise analyses in standardized MNI space. In the first step, NM-MRI scans and T2-weighted scans were coregistered to T1-weighted scans. Tissue segmentation was performed using T1- and T2-weighted scans as separate channels (segmentation was performed based solely on the T1-weighted scan for 15 psychosis controls, 1 PD patient, and 2 schizophrenia patients missing T2-weighted scans). Scans from all study participants were normalized into MNI space using DARTEL routines (71) with a gray- and white-matter template generated from an initial sample of 40 individuals (20 schizophrenia patients and 20 controls). The resampled voxel size of unsmoothed, normalized NM-MRI scans was 1 mm, isotropic. All images were visually inspected after each preprocessing step. See Fig. 2C and *SI Appendix*, Fig. S1 for quality checks of spatial normalization. Intensity normalization and spatial smoothing were then performed using custom Matlab scripts. CNR for each subject and voxel v was calculated as the relative change in NM-MRI signal intensity I from a reference region RR of white-matter tracts known to have minimal NM content, the crus cerebri, as: $CNR_v = (I_v - mode(I_{RR}))/mode(I_{RR})$. A template mask of the reference region in MNI space (Fig. 2B) was created by manual tracing on a template NM-MRI image (an average of normalized NM-MRI scans from the initial sample of 40 individuals, see Fig. 2A). The $mode(I_{RR})$ was calculated for each participant from kernel-smoothing-function fit of a histogram of all voxels in the mask. We employed the mode rather than mean or median because we found it was more robust to outlier voxels (e.g., due to edge artifacts), alleviating any need for further modification of the reference-region mask. Images were then spatially smoothed with a 1-mm full-width-at-half-maximum Gaussian kernel. Finally, an overinclusive mask of SN voxels was created by manual tracing on the template NM-MRI image. The mask was subsequently reduced by eliminating edge voxels with extreme values: voxels showing extreme relative values for a given participant (beyond the first or the 99th percentile of the CNR distribution across SN voxels in more than two subjects) or voxels showing consistently low signal across participants (CNR less than 5% in more than 90% of subjects). These procedures removed 9% of the voxels in the manually traced mask, leaving a final template SN mask containing 1,807 resampled voxels (Fig. 2B).

NM-MRI Analysis. All analyses were carried out in Matlab (Mathworks) using custom scripts. In general, robust linear regression analyses were performed across subjects for every voxel v within the SN mask, as:

$$CNR_v = \beta_0 + \beta_1 \cdot measure\ of\ interest + \sum_{i=2}^{n} \beta_i \cdot nuisance\ covariate + \varepsilon.$$

The measure of interest consisted of either imaging (e.g., dopamine-release capacity) or clinical (e.g., psychosis severity) data, depending on the analysis. Nuisance covariates, including diagnosis, head coil, and age, varied for different analyses; while all analyses included an age covariate, head coil and diagnosis covariates were only included in analyses where these variables differed across subjects. Robust linear regression was used to minimize the need for regression diagnostics in the context of mass-univariate, voxelwise analyses. A partial (nonparametric) Spearman correlation was used instead of linear regression if variables were not normally distributed according to a Lilliefors test at $P < 0.05$ (which was the case for dopamine-release capacity). Voxelwise analyses were carried out within the template SN mask after censoring subject data points with missing values (due to incomplete coverage of the dorsal SN in a minority of subjects resulting from interindividual variability in anatomy) or extreme values [values more extreme than the first or the 99th percentile of the CNR distribution across all SN voxels and subjects (CNR values below −9% or above 40%, respectively)]. For all voxelwise analyses, the spatial extent of an effect was defined as the number of voxels k (adjacent or nonadjacent) exhibiting a significant relationship between the measure of interest and CNR (voxel-level height threshold for t test of regression coefficient β_1 of $P < 0.05$, one-sided [β_1^*]). Hypothesis testing was based on a permutation test in which the measure of interest was randomly shuffled with respect to CNR. This test corrected for multiple comparisons by determining whether an effect's spatial extent k was greater than would be expected by chance [$P_{corrected} < 0.05$; 10,000 permutations; equivalent to a cluster-level familywise error-corrected P value, although in this case, voxels were not required to form a cluster of adjacent voxels, given the small size of the SN and evidence that SN tiers defined by specific projection sites do not necessarily comprise anatomically clustered neurons (23)]. On each iteration, the order of the values of a variable of interest (e.g., dopamine-release capacity) was randomly permuted across subjects (and maintained for the analysis of every voxel within the SN mask for a given iteration of the permutation test, accounting for spatial dependencies). This provided a measure of spatial extent for each of 10,000 permuted datasets, forming a null distribution against which to calculate the probability of observing the spatial extent k of the effect in the true data by chance ($P_{corrected}$). For hypothesis testing related to conjunction effects (e.g., overlap of psychosis effects in the two clinical groups), permutation analyses determined if the extent k of overlap for both effects ($\beta_{1\ effect1}^* \cap \beta_{1\ effect2}^*$) was greater than would be expected by chance ($P < 0.05$; 10,000 permutations) based on a null distribution counting the overlap of significant voxels after the location of true significant voxels for each effect was randomly shuffled within the SN mask.

Topographical analyses. Multiple-linear regression analysis across SN voxels was used to predict the strength of an effect (or the presence of a significant conjunction effect) as a function of MNI voxel coordinates in the x (absolute distance from the midline), y, and z directions.

ROI analyses. ROI analyses examining mean NM-MRI signal across voxels in the whole SN mask included the same covariates as used in the respective voxelwise analyses plus an additional dummy covariate indexing subjects with incomplete coverage of dorsal SN, as a dorsal–ventral gradient of signal intensity in SN biased mean CNR values in these subjects. This "incomplete SN coverage" covariate was not necessary for analyses on NM-MRI signal extracted from "dopamine" voxels or "psychosis-overlap" voxels as these confined sets of voxels had a relatively small contribution from dorsal SN. Partial correlation coefficients from analyses including mean NM-MRI signal (from the whole SN ROI or from sets of voxels identified via voxelwise analysis) were reported, together with their 95% CIs, calculated using bootstrapping.

Postmortem Experiment. Postmortem specimens of human midbrain tissue were obtained from The New York Brain Bank at Columbia University. Seven specimens were obtained, each from an individual who suffered from Alzheimer's disease or other non-PD dementia at the time of death (ages 44–90 y; for further clinical and demographic information, see *SI Appendix*, Table S1). Specimens were ~3-mm-thick slices of fresh frozen tissue from the rostral hemimidbrain containing pigmented SN. These specimens were scanned using the NM-MRI protocol similar to the one used in vivo, after which they were dissected for analyses of NM tissue concentration (*SI Appendix*). The dish containing the specimen included a grid insert, used to keep dissections in register with MR images.

Neurochemical measurement of NM concentration in postmortem tissue. Samples deriving from each grid section were carefully homogenized with titanium tools. NM concentration of each grid section was then measured according to our previously described spectrophotometry method (17), with minor

NEUROSCIENCE

modifications to improve the removal of interfering tissue components from midbrain regions with higher content of fibers and fewer NM-containing neurons compared with sections of SN proper dissected along anatomical boundaries. Additional tests confirmed that our methods for Fomblin cleaning were effective and that neither this substance nor the methylene blue dye was likely to influence spectrophotometric measurements of NM (*SI Appendix*). Data from 2% of grid sections (2 out of 118) could not be used due to technical problems with dissection, handling, or measurement.

MRI measurement of NM signal in postmortem tissue. NM-MRI signal was measured in corresponding grid sections using a custom Matlab script. Processing of NM-MRI images included automated removal of voxels showing edge artifacts and signal dropout (*SI Appendix*), averaging over slices to create a 2D image, and registration with a grid of dimensions matching the grid insert. The grid registration was adjusted manually based on the well markers and grid-shaped edge artifacts present in the superior-most slice where the grid insert rested. Signal in the remaining voxels was averaged within each grid section. To normalize signal intensity across specimens, CNR for each grid section was calculated as in the in vivo voxelwise analyses (see *NM-MRI Preprocessing*). The reference region for each specimen was defined by the three grid sections that best matched the location of the crus cerebri reference region used for in vivo scanning.

Statistical analysis of postmortem data. A generalized linear mixed-effects model including data across all grid sections g and specimens s was used to predict NM tissue concentration in each grid section based on mean NM-MRI CNR in the same grid section (see *SI Appendix* for details).

PET Imaging Study. Eighteen subjects without neurodegenerative illness (nine healthy controls, nine unmedicated schizophrenia patients) underwent PET scanning using the radiotracer [^{11}C]raclopride and an amphetamine challenge to quantify dopamine-release capacity (see *SI Appendix* for further details). All of these subjects also participated in the psychosis study and are described in the corresponding section below. A baseline (preamphetamine) PET scan was conducted on one day, and a postamphetamine PET scan was acquired the next day [see Weinstein et al. (72) for detailed methods], 5–7 h after administration of dextroamphetamine (0.5 mg/kg, PO). *SI Appendix, Table S3* shows PET scan parameters and characteristics of participants in the PET study. For each PET scan, list-mode data were acquired on a Biograph mCT PET-CT scanner (Siemens/CTI) over 60 min following a single-bolus injection of [^{11}C]raclopride, binned into a sequence of frames of increasing duration and reconstructed by filtered back projection using manufacturer-provided software. PET data were motion-corrected and registered to the individuals' T1-weighted MRI scan (see *NM-MRI Acquisition* and *NM-MRI Preprocessing*) using SPM2. ROIs were drawn on each subject's T1-weighted MRI scan and transferred to the coregistered PET data. Time–activity curves were formed as the mean activity in each ROI in each frame. In line with our hypothesis, our a priori ROI was the associative striatum, defined as the entire caudate nucleus and the precommissural putamen (33, 73), a part of the dorsal striatum that receives nigrostriatal axonal projections from SN neurons (22, 23) and that has been consistently implicated in psychosis (23). Data were analyzed using the simplified reference-tissue model (74, 75) with cerebellum as a reference tissue to determine the binding potential relative to the nondisplaceable compartment (BP$_{ND}$). The primary outcome measure was the relative reduction in BP$_{ND}$ (ΔBP$_{ND}$), reflecting amphetamine-induced dopamine release, a measure of dopamine-release capacity. Amphetamine induces synaptic release of dopamine derived from both cytosolic and vesicular stores (31). This results in excessive competition with the radiotracer at the D2 receptor, and, simultaneously, agonist-induced D2-receptor internalization, both of which cause radiotracer displacement and

lower BP$_{ND}$ (23, 76–78). ΔBP$_{ND}$ thus combines both effects and reflects the magnitude of dopamine stores. Since these stores depend on dopamine synthesis, the dopamine-release capacity PET measure is relevant to dopamine function. It is also relevant to NM given that NM accumulation can be driven by cytosolic dopamine (or by vesicular dopamine once it is transported into the cytosol) (6, 10, 19).

ASL Perfusion Imaging Study. Thirty-one subjects without neurodegenerative illness [12 healthy controls; 19 schizophrenia patients; 74% male (23/31); mean age, 32 y] underwent ASL-fMRI scanning at rest to quantify regional CBF. All of these subjects also participated in the psychosis study. Three-dimensional pseudocontinuous ASL perfusion imaging was performed using a 3D background suppressed fast spin-echo stack-of-spiral readout module with eight in-plane spiral interleaves (TR = 4,463 ms; TE = 10.2 ms; labeling duration = 1,500 ms; postlabeling delay = 2,500 ms; no flow-crushing gradients; FoV = 240 × 240; NEX = 3; slice thickness = 4 mm) and an echo train length of 23 to obtain 23 consecutive axial slices. A labeling plane of 10-mm thickness was placed 20 mm inferior to the lower edge of the cerebellum. Total scan time was 259 s. The ASL perfusion data were analyzed to create CBF images using Functool software (version 9.4; GE Medical Systems). CBF was calculated as in prior work (79) (*SI Appendix*). For preprocessing, CBF images were coregistered to ASL-localizer images, which were then coregistered to T1 images, with the coregistration parameters applied to CBF images. CBF images were then normalized into MNI space using the same procedures described above for NM-MRI scans. Mean CBF was calculated within the whole SN mask and within the mask of SN voxels significantly related to dopamine-release capacity in the associative striatum. ROI-based partial correlation analyses tested the relationship between mean CBF and mean NM-MRI CNR in the same mask, controlling for age and diagnosis.

Psychosis Study. Thirty-three unmedicated patients with schizophrenia and 25 individuals at CHR for psychosis participated in the study. We also included healthy controls for exploratory comparison purposes: one group ($n = 30$) age-matched to the schizophrenia group and another ($n = 15$) age-matched to the CHR group. See *SI Appendix, Supplementary Information Text* and *Table S5* for demographic and clinical information for all relevant groups.

Data Availability Statement. Raw data for this manuscript and Matlab scripts will be available upon request.

1. Abi-Dargham A, Horga G (2016) The search for imaging biomarkers in psychiatric disorders. *Nat Med* 22:1248–1255.
2. Zecca L, et al. (2008) New melanic pigments in the human brain that accumulate in aging and block environmental toxic metals. *Proc Natl Acad Sci USA* 105:17567–17572.
3. Zucca FA, et al. (2014) Neuromelanin of the human substantia nigra: An update. *Neurotox Res* 25:13–23.
4. Zucca FA, et al. (2018) Neuromelanin organelles are specialized autolysosomes that accumulate undegraded proteins and lipids in aging human brain and are likely involved in Parkinson's disease. *NPJ Parkinsons Dis* 4:17.
5. Zhang W, et al. (2011) Neuromelanin activates microglia and induces degeneration of dopaminergic neurons: Implications for progression of Parkinson's disease. *Neurotox Res* 19:63–72.
6. Zucca FA, et al. (2017) Interactions of iron, dopamine and neuromelanin pathways in brain aging and Parkinson's disease. *Prog Neurobiol* 155:96–119.
7. Zecca L, et al. (2004) The role of iron and copper molecules in the neuronal vulnerability of locus coeruleus and substantia nigra during aging. *Proc Natl Acad Sci USA* 101:9843–9848.

8. Sasaki M, et al. (2006) Neuromelanin magnetic resonance imaging of locus ceruleus and substantia nigra in Parkinson's disease. *Neuroreport* 17:1215–1218.
9. Trujillo P, et al. (2017) Contrast mechanisms associated with neuromelanin-MRI. *Magn Reson Med* 78:1790–1800.
10. Sulzer D, et al. (2018) Neuromelanin detection by magnetic resonance imaging (MRI) and its promise as a biomarker for Parkinson's disease. *NPJ Parkinsons Dis* 4:11.
11. Tosk JM, et al. (1992) Effects of the interaction between ferric iron and L-dopa melanin on T1 and T2 relaxation times determined by magnetic resonance imaging. *Magn Reson Med* 26:40–45.
12. Kuya K, et al. (2016) Correlation between neuromelanin-sensitive MR imaging and (123)I-FP-CIT SPECT in patients with parkinsonism. *Neuroradiology* 58:351–356.
13. Fabbri M, et al. (2017) Substantia nigra neuromelanin as an imaging biomarker of disease progression in Parkinson's disease. *J Parkinsons Dis* 7:491–501.
14. Hatano T, et al. (2017) Neuromelanin MRI is useful for monitoring motor complications in Parkinson's and PARK2 disease. *J Neural Transm (Vienna)* 124:407–415.
15. Matsuura K, et al. (2013) Neuromelanin magnetic resonance imaging in Parkinson's disease and multiple system atrophy. *Eur Neurol* 70:70–77.

16. Hirsch E, Graybiel AM, Agid YA (1988) Melanized dopaminergic neurons are differentially susceptible to degeneration in Parkinson's disease. *Nature* 334:345–348.
17. Zecca L, et al. (2002) The absolute concentration of nigral neuromelanin, assayed by a new sensitive method, increases throughout the life and is dramatically decreased in Parkinson's disease. *FEBS Lett* 510:216–220.
18. Cebrián C, et al. (2014) MHC-I expression renders catecholaminergic neurons susceptible to T-cell-mediated degeneration. *Nat Commun* 5:3633.
19. Sulzer D, et al. (2000) Neuromelanin biosynthesis is driven by excess cytosolic catecholamines not accumulated by synaptic vesicles. *Proc Natl Acad Sci USA* 97:11869–11874.
20. Shibata E, et al. (2008) Use of neuromelanin-sensitive MRI to distinguish schizophrenic and depressive patients and healthy individuals based on signal alterations in the substantia nigra and locus ceruleus. *Biol Psychiatry* 64:401–406.
21. Watanabe Y, et al. (2014) Neuromelanin magnetic resonance imaging reveals increased dopaminergic neuron activity in the substantia nigra of patients with schizophrenia. *PLoS One* 9:e104619.
22. Joel D, Weiner I (2000) The connections of the dopaminergic system with the striatum in rats and primates: An analysis with respect to the functional and compartmental organization of the striatum. *Neuroscience* 96:451–474.
23. Weinstein JJ, et al. (2017) Pathway-specific dopamine abnormalities in schizophrenia. *Biol Psychiatry* 81:31–42.
24. Rice MW, Roberts RC, Melendez-Ferro M, Perez-Costas E (2016) Mapping dopaminergic deficiencies in the substantia nigra/ventral tegmental area in schizophrenia. *Brain Struct Funct* 221:185–201.
25. Chung CY, et al. (2005) Cell type-specific gene expression of midbrain dopaminergic neurons reveals molecules involved in their vulnerability and protection. *Hum Mol Genet* 14:1709–1725.
26. Verney C, Zecevic N, Puelles L (2001) Structure of longitudinal brain zones that provide the origin for the substantia nigra and ventral tegmental area in human embryos, as revealed by cytoarchitecture and tyrosine hydroxylase, calretinin, calbindin, and GABA immunoreactions. *J Comp Neurol* 429:22–44.
27. Damier P, Hirsch EC, Agid Y, Graybiel AM (1999) The substantia nigra of the human brain. II. Patterns of loss of dopamine-containing neurons in Parkinson's disease. *Brain* 122:1437–1448.
28. Fearnley JM, Lees AJ (1991) Ageing and Parkinson's disease: Substantia nigra regional selectivity. *Brain* 114:2283–2301.
29. Bogerts B, Häntsch J, Herzer M (1983) A morphometric study of the dopamine-containing cell groups in the mesencephalon of normals, Parkinson patients, and schizophrenics. *Biol Psychiatry* 18:951–969.
30. Langley J, Huddleston DE, Liu CJ, Hu X (2017) Reproducibility of locus coeruleus and substantia nigra imaging with neuromelanin sensitive MRI. *MAGMA* 30:121–125.
31. Sulzer D (2011) How addictive drugs disrupt presynaptic dopamine neurotransmission. *Neuron* 69:628–649.
32. Sulzer D, Cragg SJ, Rice ME (2016) Striatal dopamine neurotransmission: Regulation of release and uptake. *Basal Ganglia* 6:123–148.
33. Kegeles LS, et al. (2010) Increased synaptic dopamine function in associative regions of the striatum in schizophrenia. *Arch Gen Psychiatry* 67:231–239.
34. Cha YH, et al. (2013) Regional correlation between resting state FDG PET and pCASL perfusion MRI. *J Cereb Blood Flow Metab* 33:1909–1914.
35. Chen Y, et al. (2011) Voxel-level comparison of arterial spin-labeled perfusion MRI and FDG-PET in Alzheimer disease. *Neurology* 77:1977–1985.
36. Detre JA, Rao H, Wang DJ, Chen YF, Wang Z (2012) Applications of arterial spin labeled MRI in the brain. *J Magn Reson Imaging* 35:1026–1037.
37. Schridde U, et al. (2008) Negative BOLD with large increases in neuronal activity. *Cereb Cortex* 18:1814–1827.
38. Hermes M, et al. (2009) Latent state-trait structure of cerebral blood flow in a resting state. *Biol Psychol* 80:196–202.
39. Egerton A, et al. (2013) Presynaptic striatal dopamine dysfunction in people at ultra-high risk for psychosis: Findings in a second cohort. *Biol Psychiatry* 74:106–112.
40. Howes OD, et al. (2011) Dopamine synthesis capacity before onset of psychosis: A prospective [18F]-DOPA PET imaging study. *Am J Psychiatry* 168:1311–1317.
41. Jauhar S, et al. (2017) A test of the transdiagnostic dopamine hypothesis of psychosis using positron emission tomographic imaging in bipolar affective disorder and schizophrenia. *JAMA Psychiatry* 74:1206–1213.
42. Endres CJ, et al. (1997) Kinetic modeling of [11C]raclopride: Combined PET-microdialysis studies. *J Cereb Blood Flow Metab* 17:932–942.
43. Laruelle M, et al. (1997) Microdialysis and SPECT measurements of amphetamine-induced dopamine release in nonhuman primates. *Synapse* 25:1–14.
44. Kay SR, Fiszbein A, Opler LA (1987) The positive and negative syndrome scale (PANSS) for schizophrenia. *Schizophr Bull* 13:261–276.
45. Kay SR, Opler LA, Lindenmayer JP (1988) Reliability and validity of the positive and negative syndrome scale for schizophrenics. *Psychiatry Res* 23:99–110.
46. Kitao S, et al. (2013) Correlation between pathology and neuromelanin MR imaging in Parkinson's disease and dementia with Lewy bodies. *Neuroradiology* 55:947–953.
47. Lee H, Baek SY, Chun SY, Lee JH, Cho H (2018) Specific visualization of neuromelanin-iron complex and ferric iron in the human post-mortem substantia nigra using MR relaxometry at 7T. *Neuroimage* 172:874–885.
48. Ito H, et al. (2017) Normative data of dopaminergic neurotransmission functions in substantia nigra measured with MRI and PET: Neuromelanin, dopamine synthesis, dopamine transporters, and dopamine D₂ receptors. *Neuroimage* 158:12–17.
49. Brown CA, et al. (2013) Validation of midbrain positron emission tomography measures for nigrostriatal neurons in macaques. *Ann Neurol* 74:602–610.
50. Howes OD, et al. (2013) Midbrain dopamine function in schizophrenia and depression: A post-mortem and positron emission tomographic imaging study. *Brain* 136:3242–3251.
51. Mueller HT, Haroutunian V, Davis KL, Meador-Woodruff JH (2004) Expression of the ionotropic glutamate receptor subunits and NMDA receptor-associated intracellular proteins in the substantia nigra in schizophrenia. *Brain Res Mol Brain Res* 121:60–69.
52. Perez-Costas E, Melendez-Ferro M, Rice MW, Conley RR, Roberts RC (2012) Dopamine pathology in schizophrenia: Analysis of total and phosphorylated tyrosine hydroxylase in the substantia nigra. *Front Psychiatry* 3:31.
53. Laruelle M, Abi-Dargham A, Gil R, Kegeles L, Innis R (1999) Increased dopamine transmission in schizophrenia: Relationship to illness phases. *Biol Psychiatry* 46:56–72.
54. Sasaki M, et al. (2010) Visual discrimination among patients with depression and schizophrenia and healthy individuals using semiquantitative color-coded fast spin-echo T1-weighted magnetic resonance imaging. *Neuroradiology* 52:83–89.
55. Yamashita F, et al. (2016) Detection of changes in the ventral tegmental area of patients with schizophrenia using neuromelanin-sensitive MRI. *Neuroreport* 27:289–294.
56. Kim E, et al. (2017) Presynaptic dopamine capacity in patients with treatment-resistant schizophrenia taking clozapine: An [18F]DOPA PET study. *Neuropsychopharmacology* 42:941–950.
57. Chen S, Seeman P, Liu F (2011) Antipsychotic drug binding in the substantia nigra: An examination of high metoclopramide binding in the brains of normal, Alzheimer's disease, Huntington's disease, and multiple sclerosis patients, and its relation to tardive dyskinesia. *Synapse* 65:119–124.
58. McGlashan TH, et al. (2006) Randomized, double-blind trial of olanzapine versus placebo in patients prodromally symptomatic for psychosis. *Am J Psychiatry* 163:790–799.
59. McGorry PD, et al. (2002) Randomized controlled trial of interventions designed to reduce the risk of progression to first-episode psychosis in a clinical sample with subthreshold symptoms. *Arch Gen Psychiatry* 59:921–928.
60. Cannon TD, et al. (2016) An individualized risk calculator for research in prodromal psychosis. *Am J Psychiatry* 173:980–988.
61. Wakamatsu K, et al. (2015) Norepinephrine and its metabolites are involved in the synthesis of neuromelanin derived from the locus coeruleus. *J Neurochem* 135:768–776.
62. Clewett DV, Huang R, Velasco R, Lee TH, Mather M (2018) Locus coeruleus activity strengthens prioritized memories under arousal. *J Neurosci* 38:1558–1574.
63. Mather M, et al. (2017) Higher locus coeruleus MRI contrast is associated with lower parasympathetic influence over heart rate variability. *Neuroimage* 150:329–335.
64. Weinshenker D (2018) Long road to ruin: Noradrenergic dysfunction in neurodegenerative disease. *Trends Neurosci* 41:211–223.
65. Clewett DV, et al. (2016) Neuromelanin marks the spot: Identifying a locus coeruleus biomarker of cognitive reserve in healthy aging. *Neurobiol Aging* 37:117–126.
66. Hämmerer D, et al. (2018) Locus coeruleus integrity in old age is selectively related to memories linked with salient negative events. *Proc Natl Acad Sci USA* 115:2228–2233.
67. Reuter M, et al. (2015) Head motion during MRI acquisition reduces gray matter volume and thickness estimates. *Neuroimage* 107:107–115.
68. Root DH, et al. (2016) Glutamate neurons are intermixed with midbrain dopamine neurons in nonhuman primates and humans. *Sci Rep* 6:30615.
69. Zhang Y, Larcher KM, Misic B, Dagher A (2017) Anatomical and functional organization of the human substantia nigra and its connections. *eLife* 6:e26653.
70. Chen X, et al. (2014) Simultaneous imaging of locus coeruleus and substantia nigra with a quantitative neuromelanin MRI approach. *Magn Reson Imaging* 32:1301–1306.
71. Ashburner J (2007) A fast diffeomorphic image registration algorithm. *Neuroimage* 38:95–113.
72. Weinstein JJ, et al. (2018) PET imaging of dopamine-D2 receptor internalization in schizophrenia. *Mol Psychiatry* 23:1506–1511.
73. Martinez D, et al. (2003) Imaging human mesolimbic dopamine transmission with positron emission tomography. Part II: Amphetamine-induced dopamine release in the functional subdivisions of the striatum. *J Cereb Blood Flow Metab* 23:285–300.
74. Lammertsma AA, Hume SP (1996) Simplified reference tissue model for PET receptor studies. *Neuroimage* 4:153–158.
75. Mawlawi O, et al. (2001) Imaging human mesolimbic dopamine transmission with positron emission tomography: I. Accuracy and precision of D(2) receptor parameter measurements in ventral striatum. *J Cereb Blood Flow Metab* 21:1034–1057.
76. Guo N, et al. (2010) Impact of D2 receptor internalization on binding affinity of neuroimaging radiotracers. *Neuropsychopharmacology* 35:806–817.
77. Ito K, Haga T, Lameh J, Sadée W (1999) Sequestration of dopamine D2 receptors depends on coexpression of G-protein-coupled receptor kinases 2 or 5. *Eur J Biochem* 260:112–119.
78. Skinbjerg M, et al. (2010) D2 dopamine receptor internalization prolongs the decrease of radioligand binding after amphetamine: A PET study in a receptor internalization-deficient mouse model. *Neuroimage* 50:1402–1407.
79. Wong AM, Yan FX, Liu HL (2014) Comparison of three-dimensional pseudocontinuous arterial spin labeling perfusion imaging with gradient-echo and spin-echo dynamic susceptibility contrast MRI. *J Magn Reson Imaging* 39:427–433.